The role of the Co^{2+}/Co^{3+} redox-pair in the properties of $La_{2-x}Sr_xCoTiO_6$ $(0 \leq x \leq 0.5)$ perovskites as components for solid oxide fuel cells

Alejandro Gómez-Pérez [a], Mercedes Yuste [a], Juan Carlos Pérez-Flores [a,*], Clemens Ritter [b],
M. Teresa Azcondo [a], Jesús Canales-Vázquez [c], María Gálvez-Sánchez [c], Khalid Boulahya [d],
Flaviano García-Alvarado [a], Ulises Amador [a]

[a] Dpto. Química, Facultad de Farmacia, Universidad CEU San Pablo, Urb. Montepríncipe, Boadilla del Monte, E-28668 Madrid, Spain
[b] Institut Laue-Langevin, BP 156-38042 Grenoble Cedex 9, France
[c] Renewable Energy Institute, Universidad Castilla-La Mancha, E-02006 Albacete, Spain
[d] Dpto. Química Inorgánica, Facultad Ciencias Químicas, Universidad Complutense, E-28040 Madrid, Spain

HIGHLIGHTS

► $La_{2-x}Sr_xCoTiO_6$ exhibits good conductivity and electrochemical activity under air conditions.
► The Co^{2+}/Co^{3+} redox pair plays a significant role in the electronic transport mechanism.
► Microstructural features (short-range ordering) are decisive for the electrical conductivity.
► All these make them potentially useful as components of composite cathode of SOFCs.

ARTICLE INFO

ABSTRACT

Substitution of La^{3+} by Sr^{2+} in the perovskite La_2CoTiO_6 yields materials of the $La_{2-x}Sr_xCoTiO_6$ series. The dominant charge-compensating mechanism is oxidation of Co^{2+} if they are prepared at air. The as prepared oxides can be reduced inducing a large amount of oxygen vacancies while keeping the perovskite structure. The electrical behaviour of the $La_{2-x}Sr_xCoTiO_6$ series is dominated by p-type electronic conduction in a wide pO_2 range through non-adiabatic hopping of small-polarons. The electrical conductivity increases with x, except for the $x = 0.5$ material which shows an unexpectedly low conductivity due to microstructural and short-range ordering effects. The highest conductivity material, $La_{1.60}Sr_{0.40}CoTiO_6$, is selected to study the electrochemical properties of the series. This compound is chemically compatible with YSZ up to 1373 K, in both oxidizing and reducing atmospheres. The preliminary evaluation of the electrode performance reveals that $La_{1.60}Sr_{0.40}CoTiO_6$-based electrodes exhibit polarization resistances of typically 0.8 Ω cm² at 1073 K in oxygen, which are close to the values obtained for LSM-based cathodes. Thus, the electrochemical behaviour of this oxide as cathode is particularly encouraging since the electrode microstructure is not optimized; it is expected that an improved microstructure will perform at least similarly to the state-of-art in SOFCs materials.

1. Introduction

Perovskite-like materials constitute one of the most versatile families of compounds in the field of solid state chemistry. There are many possibilities to improve and tune their physical properties such as electrical (electronic and ionic) conductivity, catalytic activity, thermal expansion control, thermoelectric and magnetic behaviour, etc by changing the chemical composition through aliovalent substitution and/or doping. Therefore, perovskite oxides (with formula ABO_3) are very attractive materials for technological applications as solid oxide fuel cells (SOFCs), oxygen sensors, thermoelectric power generators and other electrochemical devices.

In the framework of the research on materials for solid oxide fuel cells (SOFCs), the possibility to modulate and change the

electrical and electrochemical characteristics of perovskite-like oxides by substitution in the A-site by a cation with lower oxidation state appears as an easy and attractive option. This may lead to an enhancement of the ionic conductivity due to the formation of mobile oxygen vacancies, and/or the improvement of electronic conduction by inducing mixed oxidation states of B-cation. Both are desirable properties for mixed ionic−electronic conductors (MIECs) and therefore, for SOFC electrodes [1,2].

Among perovskite-type oxides, cobaltites have attracted a continued attention due to their excellent electronic transport properties [3] and mixed ionic−electronic conductivity which make them a potential alternative to present state-of-art SOFC cathode material, $La_{1-x}Sr_xMnO_{3-\delta}$, (LSM hereafter) [4,5]. Interestingly, either n- or p-type conductivity can be induced in cobaltites by an appropriate doping or substitution in the B-site [6]. Substitution in A-site offers a more complex way to modify the conduction mechanisms. As an example, in $La_{1-x}Sr_xCoO_{3-\delta}$, the operating temperature plays a determinant role in the conduction properties. At low temperature the oxidation of cobalt is the main charge compensation mechanism for the aliovalent La^{3+} by Sr^{2+} substitution, and therefore p-type conductivity is observed. On the contrary, the reducing effect associated to high temperature induces the reduction of trivalent cobalt and the creation of oxygen vacancies [7−9]. The conductivity of these compounds was measured as a function of oxygen partial pressure (pO_2). They showed p-type conductivity based on a small-polaron hopping mechanism with a possible metal−insulator transition at pO_2 lower than 10^{-3} atm [10−12]. Ionic conductivity, which is attributed to oxygen-vacancies diffusion under a chemical or electrical gradient [13], is also present in these compounds. Its independence on the pO_2 is explained as a counterbalance of vacancy formation and defect ordering [14,15].

The interest on cobalt-based oxides has spread to double perovskites and several recent studies report on the remarkable properties of these compounds [16−18].

This paper presents a detailed structural and electrical characterization of the double perovskite $La_{2-x}Sr_xCoTiO_6$ series, $0 \le x \le 0.5$. The use of neutron powder diffraction combined with transmission microscopy and electron diffraction provides a detailed structural characterization of these materials, which allows explaining their electrical properties. A preliminary electrochemical study of these materials as electrodes for SOFCs reveals that performance is similar to the best state-of-the-art materials, LSM for instance.

2. Experimental procedure

2.1. Samples synthesis

Samples of composition $La_{2-x}Sr_xCoTiO_6$ ($0 \le x \le 0.5$) were prepared by a modified Pechini method as described by Yuste et al. [19]. Reduced samples have been obtained by heating the former at 1173 K overnight (2 K min^{-1}) under a dry 5%H$_2$:Ar flow, (pO_2 $\sim 10^{-21}$ atm), and cooling down to room temperature (RT) while keeping the gas flux.

2.2. Experimental techniques

Purity and structure of the samples were determined by powder X-ray diffraction (XRD) on a Bruker D8 high-resolution diffractometer, using monochromatic CuK$_{\alpha 1}$ ($\lambda = 0.15406$ nm) radiation obtained with a germanium primary monochromator, and equipped with a solid-state rapid LynxEye detector.

Selected area electron diffraction (SAED) and high resolution electron microscopy (HREM) were performed using a JEOL 3000FEG

electron microscope, fitted with a double tilting goniometer stage ($\pm 25°$, $\pm 25°$). Simulated HREM images were calculated by the multislice method using the MacTempas software package.

Neutron powder diffraction (NPD) experiments at room temperature were performed on the high resolution diffractometer D2B at the Institut Laue-Langevin. A monochromatic beam of wavelength 0.15940 nm was selected with a Ge monochromator from the primary beam the divergence of which was defined by an additional 10′ collimator to increase the instrumental resolution. The structural refinements were carried out by the Rietveld method using the FullProf program [20] by the simultaneous fitting of XRD and NPD data. The neutron scattering amplitudes used in the refinement were 0.824, 0.702, 0.249, −0.344 and 0.581 (10^{-12} cm) for La, Sr, Co, Ti and O, respectively. Prior to the structure refinements, a pattern matching without structural model was performed. This allows one to obtain suitable profile parameters and to verify the adequateness of the chosen space group. Then, the structural model was refined keeping constant the profile parameters. When needed, along the refinements, some of these profile parameters were allowed to vary; but at the final steps of the refinements they were kept constant. The refinements were stable provided the number of refined parameters describing the structural model was limited to obtain a sufficient peaks-to-parameters ratio. To ensure this, isotropic thermal factors (ITF) were used for all the atoms in the structure and some constrains were used.

Impedance spectroscopy (IS) was measured on bars (ca. 80% relative density) prepared by uniaxially pressing of powders to 100 MPa that were sintered at 1723−1773 K overnight and using a Solartron 1260 Frequency Response Analyzer by applying a 100 mV AC signal in the $10^6−10^{-1}$ Hz range over the temperature range 673−1073 K in air. The dependence of conductivity on oxygen partial pressure (pO_2) was measured on the same bars at 1123 K in a 4-point probe arrangement in a similar manner to that described in a previous work [21]. The pO_2 was monitored using an yttria-stabilized zirconia (YSZ) sensor with Pt electrodes attached to an external voltmeter. The cell was firstly equilibrated in a reducing atmosphere (5%H$_2$:Ar) over a period of more than 12 h. The gas flow was afterwards switched off and the chamber allowed to equilibrate slowly with the outside air over a period of several days. During this period the resistance of the sample was recorded for every change of log(pO_2) of 0.25.

Prior to the polarization studies, the chemical compatibility of $La_{1.60}Sr_{0.40}CoTiO_6$ (presented as an example) and YSZ, used as electrode components, was evaluated. Pellets of a mixture of these materials in a 1:1 w:w ratio were fired at 1373, 1223 and 1073 K for 15 h under either atmospheric ambient (oxidant) or 5%H$_2$:Ar (reducing) conditions. These temperatures have been chosen since they are commonly used in the processing and working of SOFCs. After the corresponding treatment the samples were checked by XRD.

For symmetrical cell measurements a slurry was prepared by mixing the as-prepared $La_{1.60}Sr_{0.40}CoTiO_6$ powder with YSZ (Tosoh) in a 1:1 w:w ratio with Decoflux™ (WB41, Zschimmer and Schwarz) as a binder. The electrodes were prepared by coating dense thick YSZ disks (1 mm) with this slurry using active areas of 1 cm^2. The resulting assemblies were fired at 1373 K for 6 h and then a Pt-based paste was deposited on top of the electrodes and fired again at 1273 K for 2 h. The electrodes microstructure was investigated using a 6490L JEOL Scanning Electron Microscope. The electrode thickness observed in the symmetrical cells was 20 μm.

The polarization measurements were performed on a two-electrode arrangement as previously described [22] using either flowing pure oxygen or 5%H$_2$:Ar atmospheres in the 1223−973 K temperature range. IS measurements of the electrochemical

cell were carried out using a 1470E Solartron Cell Test in the 10^6–10^{-1} Hz frequency range using a 50 mV of AC signal amplitude.

3. Results

3.1. Crystal structure and microstructure

3.1.1. As-prepared materials

Neutron powder diffraction data demonstrate that the structure of La_2CoTiO_6 is monoclinic (S.G. $P2_1/n$, #14) with unit cell $\sqrt{2}a_p \times \sqrt{2}a_p \times 2a_p$ (a_p refers to the unit cell parameter of the simple cubic perovskite), which corresponds to an octahedra tilting scheme $a^-a^-c^+$ (Fig. 1a) [23–25]. For this tilting scheme many perovskite-like materials present an orthorhombic symmetry (Fig. 1b, S.G. Pnma, #62), with the same diagonal unit cell [25]. The lowering in symmetry is mainly due to the ordering of Ti and Co in the B′ and B″ positions of the structure (see Table 1 of Supplementary Information, Table S1), the monoclinic angle being very close to 90°. In the orthorhombic model there is only one crystallographic site 4b (0 0 ½) for B cations, i.e. the symmetry does not allow for an ordered arrangement of the B cations. On the contrary, in the monoclinic model the 4b site of Pnma can be separated into two independent crystallographic sites, 2d (½ 0 0) and 2c (½ 0 ½), that allows an ordered arrangement of B cations.

Since the neutron scattering amplitudes of Co and Ti are significantly different, the site occupancies can be readily determined. Refinements show that Co^{2+} and Ti^{4+} are ordered in the parent compound La_2CoTiO_6 (Table S1) though some degree of intermixing or anti-site defects (AS) (∼10%) of Co and Ti on the B′ and B″ sites, respectively, is present. This is quite common in double perovskite in which the two B-ions are not very different in charge and size [21,25]. Contrary to what has been observed in the similar series $La_{2-x}Sr_xNiTiO_{6-\delta}$, which are Ni-deficient (and Ti-rich), materials in the Co-containing series are stoichiometric.

The structure changes noticeably as La^{3+} is being progressively substituted by Sr^{2+}; Co and Ti progressively intermix and for a degree of substitution of ca. 15% the symmetry changes from monoclinic to orthorhombic. For low substitution levels Co and Ti remain partially ordered, thus, $La_{1.90}Sr_{0.10}CoTiO_6$ presents monoclinic symmetry (though the β angle is very close to 90°). However, the intermixing of Co and Ti over the 2d and 2c sites clearly increases to about 17%, (Table S1). This is evidenced by the low intensity of the (011), (101) and (−101) peaks located at 20.2 (2θ) in the NPD patterns shown in Figure S1 (Figure 1 of SI). The intensity

of all these three peaks mainly depends on the difference of the scattering power residing at the B′ and B″ positions: the higher this difference the stronger these peaks. Since the scattering power of Co and Ti for X-ray is very similar, XRD is not suited for studying ordering in 3d-metal double perovskites. One has to remark that these peaks are noticeably broadened, suggesting that the remaining Ti/Co ordering is limited to a short-range scale, or at least is not long-range. A similar situation was found for the similar Ni-containing series previously studied [21]. From the integral breadths of the peaks (obtained by deconvolution − not shown - of the broad peak centred at 20.2 (2θ) in Figure S1b) and using the Scherrer formula the size of the ordering domains was estimated to be of ca. 17.5 nm diameter assuming a spherical shape. This value is much larger than the one observed in the equivalent member $x = 0.10$ of the $La_{2-x}Sr_xNiTiO_{6-\delta}$ system. More interestingly, as will be shown, local or short-range ordering effects are common in the title series, as SAED experiments revealed for the $x = 0.50$ member. This kind of local ordering has also been reported for other double perovskite materials such as Sr_2FeMoO_6 in which local order is preserved in samples with no detectable long-range chemical order [26]. In our materials, the random distribution of Sr and La (and eventually the oxygen vacancies this aliovalent substitution will originate) provides the driven force for disordering Co and Ti. For increasing Sr-contents, but still in the monoclinic "ordered" domain (i.e. $x \leq 0.20$ in $La_{2-x}Sr_xCoTiO_6$) refinement results indicated that the intermixing of Co and Ti increases (it is ca. 44% in this compound). Besides, the ordering domain-size diameter progressively decreases; it was estimated 7.5 nm for $x = 0.20$.

For the oxides with higher Sr-contents no evidence of Co/Ti order was observed; thus the symmetry Pnma was used in the final structure model for these materials.

In Fig. 2 the graphic result of the fitting of NPD data to the model on Table S2 for $x = 0.30$ is depicted; whereas Figure S1d shows the plot corresponding to $x = 0.50$. Although we tried the monoclinic model for this high-Sr-containing sample, the values of the agreement factors for the ordered model in $P2_1/n$ and the disordered model in Pnma were similar, the refinement in $P2_1/n$ giving a random distribution of Co and Ti among 2d and 2c sites. Thus, the orthorhombic disordered model was assumed to be correct. As for all the other compositions, either with higher or lower Sr-content, refinements revealed that the metal compositions of every sample correspond to the nominal values (Table S1).

The unit cell volume displays a continuous contraction as x increases (Fig. 3). However, this simple behaviour is the result
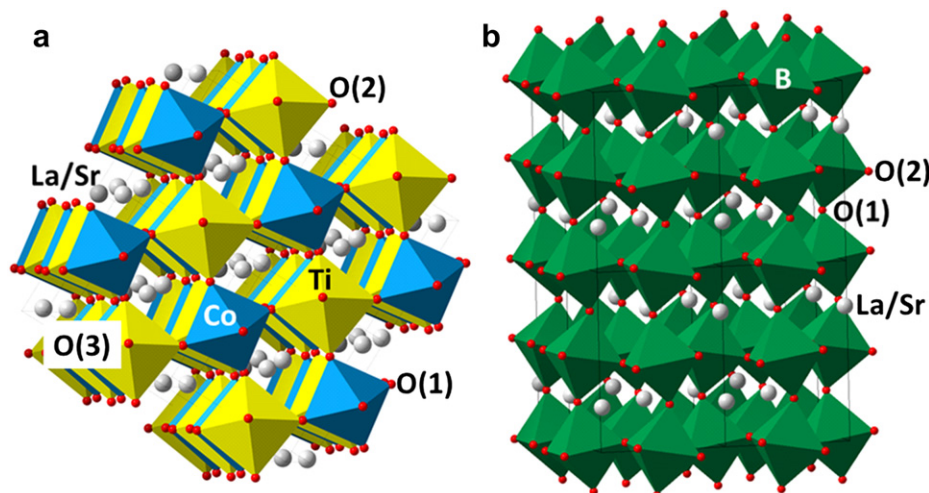

Fig. 1. Schematic representation of (a) La_2CoTiO_6 in S.G. $P2_1/n$ and (b) $La_{1.50}Sr_{0.50}CoTiO_6$ in S.G. Pnma.

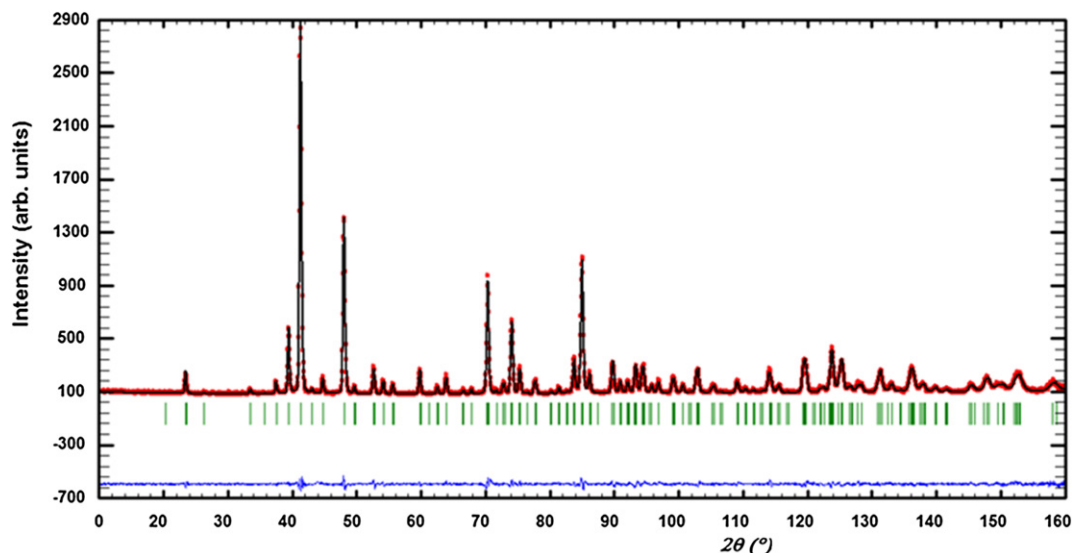**Fig. 2.** Experimental (red circles) and calculated (black continuous line) NPD patterns (and their difference, blue line at the bottom) for $La_{1.70}Sr_{0.30}CoTiO_6$ assuming S.G. Pnma. The green vertical bars indicate the positions of the Bragg peaks of this phase. (For interpretation of the references to colour in this figure legend, the reader is referred to the web version of this article.)

of a complex balance of different effects acting in opposite directions. The partial replacement of La^{3+} by a larger cation ($^{XII}r(La^{3+}) = 0.136$ nm and $^{XII}r(Sr^{2+}) = 0.144$ nm) [27] should produce a volume expansion; moreover, in ordered double perovskites a second mechanism operates in the same direction [28]. When the B-ions are partially disordered each high-valence cation (Ti^{4+} in this case) located at an AS has highly charged cations (here Ti^{4+}) as nearest-neighbour ions, as a consequence extra repulsions appear in the lattice and the cell volume should expand. This effect is expected to be more effective for disordered materials with $x \geq 0.30$. However, the molar volume clearly decreases for the "as-prepared" series (AP in Fig. 3) along the whole compositional range. This is a clear indication that aliovalent substitution must induce other effects that compensate and even overcome those two previously described. Two obvious effects are: a) oxidation of Co^{2+} to Co^{3+} and b) creation of oxygen vacancies.

Fig. 3. Unit cell volume (left axis) and trivalent cobalt content as obtained from NPD data (right axis) as a function of the strontium content, for as-prepared (AP), $La_{2-x}Sr_xCoTiO_6$, and reduced (RED), $La_{2-x}Sr_xCoTiO_{6-\delta}$, series. Lines are guides for the eye. (For interpretation of the references to colour in this figure legend, the reader is referred to the web version of this article.)

Interestingly, in a previous paper [19], magnetic measurements and chemical analyses allowed us to determine the first as the main charge-compensating mechanism, i.e. the amount of Co^{3+} in $La_{2-x}Sr_xCoTiO_{6-\delta}$ increases as the degree of aliovalent substitution does, the amount of trivalent cobalt ions corresponding almost exactly to the value of x. This is now also confirmed by the refinement of the NPD data (Table SI 1) since in Fig. 3 the concentration of Co^{3+} (calculated from the oxygen stoichiometry and assuming electro-neutrality) is well correlated to the degree of substitution.

If the substitution of La^{3+} by Sr^{2+} is compensated by the creation of oxygen-vacancies one could assume in the first thought that the process would lead to an expansion of the unit cell. Indeed, a loss of Madelung energy is induced in the material upon substitution, due to both the lowering of positive charge in the A-sites and the presence of anionic vacancies (loss of negative charges). As a result, the bonding energy decreases and the unit cell should expand. However, it is well established that in many cases more elaborated bonding models are needed to account for the effects of simple chemical modifications of oxides, such as metal substitution or creation oxygen vacancies [29]. Anyhow, NPD data demonstrate that the as-prepared compounds $La_{2-x}Sr_xCoTiO_{6-\delta}$ keep the anionic sub-structure complete ($\delta \approx 0$) with a non-detectable oxygen vacancy concentration.

Thus, the reduction of size associated to the oxidation of Co^{2+} into Co^{3+} ($^{VI}r(Co^{2+})^{LS} = 0.065$ nm and $^{VI}r(Co^{3+})^{LS} = 0.054$ nm) [27] as a result of the substitution of La^{3+} by Sr^{2+} seems to be responsible for the contraction of the unit cell. This is confirmed by the B–O distances and average BVS in Table S3; the former decreases for increasing values of x whereas the latter increases.

Selected Area Electron Diffraction (SAED) was performed in the sample corresponding to $x = 0.50$ (Fig. 4), which exhibits an anomalously low electrical conductivity (see below). The strongest spots correspond to a basic cubic perovskite cell. In Fig. 4a (taken along the [001] direction) and Fig. 4b, (along [1−21]), additional weak peaks are observed along [010], [10−1] and [111]. Thus, we can suggest that the symmetry of this phase is orthorhombic with unit cell parameters $\sqrt{2}a_p \times \sqrt{2}a_p \times 2a_p$. Indeed, all the reflections can be indexed on the basis of this orthorhombic unit cell, the reflection conditions being compatible with the Pnma (#62) space group.
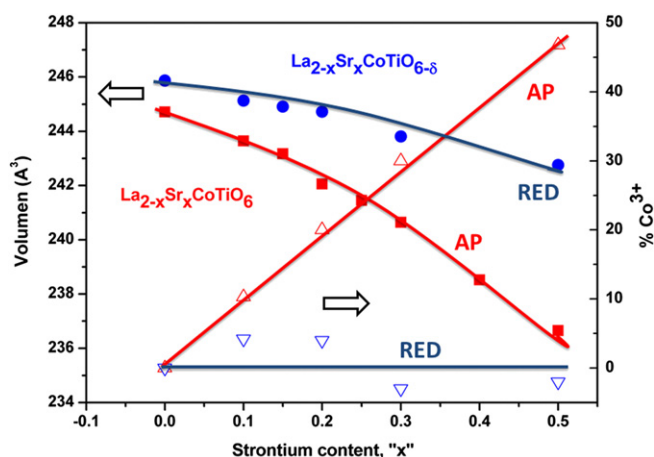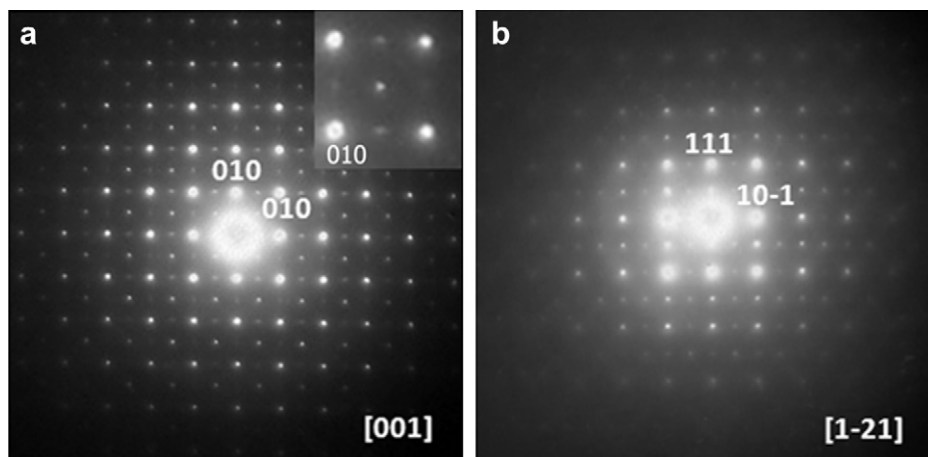
Fig. 4. SAED patterns corresponding to $La_{1.50}Sr_{0.50}CoTiO_6$ taken along $[001]p$, (a), and $[1-21]p$, (b). The indexing refers to a simple cubic unit cell $a_p \times a_p \times a_p$. The inset in (a) shows the streaking along the [010] direction.

The HREM micrograph along the $[001]p$ zone axis of $La_{1.50}Sr_{0.50}CoTiO_6$ is quite complex (Fig. 5). Although the diffraction pattern (not shown) can be indexed on the basis of a double cubic perovskite unit cell, the corresponding high-resolution image, suggests a different situation.

A careful analysis of the HREM image reveals the coexistence of two domains (A and B). Fast Fourier transform (FFT) patterns of these domains are shown in Fig. 5a and b. The first one with d-spacing of 0.38 nm corresponds to the [010] direction, whereas the d-spacings of 0.38 nm and 0.78 nm in the second one correspond to [10−1].

The presence of intergrown domains with different orientations is very common in this material. Thus, the HREM image taken along [100] (Fig. 6a) reveals the presence of different structural domains (outlined by white circles) showing d-spacing of 0.55 nm and 0.78 nm, which correspond to d_{001} and d_{010} (zone labelled by A), that intergrowth with domains associated to d-spacing of 0.28 nm and 0.78 nm, corresponding to d_{200} and d_{010} (zone labelled by B). The optical Fourier transform of these two structural domains are depicted in Fig. 6b and c, respectively. Image calculations were performed for the two domains A and B; the simulated images fit nicely to the experimental one (indicated by arrows in Fig. 6).

Besides this domain microstructure, $La_{1.50}Sr_{0.50}CoTiO_6$ oxide presents at the atomic level some other effects revealed in the SAED diagrams. Thus, the superstructure maxima doubling [010]

are elongated and some streaking along this direction is observed (inset of Fig. 4a) suggesting some degree of short-range ordering, also observed by HREM images (Figs. 5 and 6). In summary, the $x = 0.50$ member presents a very complex microstructure including short-range ordering, not observed for the other members of the series, which can account for its unexpectedly low conductivity.

3.1.2. Reduced samples

Materials to be used as a SOFC component must be stable under working conditions. Thus, anode, cathode and electrolyte materials are requested to be stable at high temperatures under reducing, oxidizing or both conditions, respectively.

Since the title compounds are prepared at high temperature in air ($pO_2 = 0.21$ atm) their stability in oxidizing environments is evident. Thus, their behaviour under reducing conditions has been
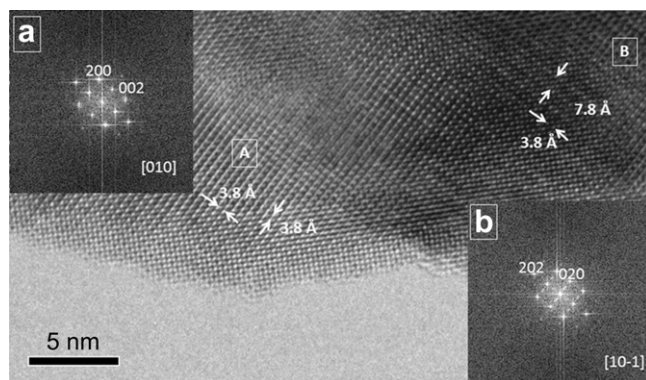

Fig. 5. HREM image of $La_{1.50}Sr_{0.50}CoTiO_6$ along $[001]p$. A twinned structure is clearly seen; (a) and (b) are optical FFTs of the domains marked A and B in the image, respectively.
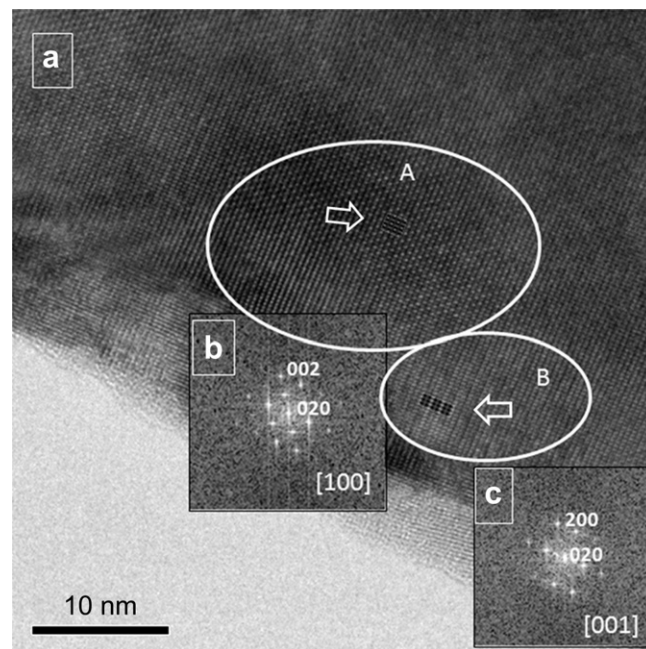

Fig. 6. HREM image of $La_{1.50}Sr_{0.50}CoTiO_6$ along $[101]p$. A twinned structure is clearly seen; (b) and (c) are optical FFTs of the domains marked as A and B in the image, respectively. The simulated images are seen at the inset ($\Delta t = 5$ nm, $\Delta f = -30$ nm).

investigated. Samples were heated overnight in dry 5%H$_2$:Ar streams and then characterized by NPD at RT. The refined structural parameters of these reduced materials have been obtained by simultaneous fitting of XRD and NPD data and are collected in Table S2 with Table S4 containing some additional structural information. As an example, Fig. 7 shows the NPD pattern for the reduced sample with the $x = 0.30$, whereas Figure S2 displays the corresponding patterns for the rest of the reduced samples of the series La$_{2-x}$SrxCoTiO$_{6-\delta}$. It is worth noting that all these oxides are stable upon reduction in the severe reducing conditions used ($pO_2 \approx 10^{-21}$ atm).

However, some important effects are induced in the materials by the reducing treatment. The most obvious one is an important expansion of the unit cell volume (Fig. 3), which is more pronounced as x increases, ranging from 0.05% to 2.6%. This is associated to a noticeable release of oxygen, (Table S2), due to the reduction of Co^{3+} to Co^{2+} (see BVS in Tables S3 and S4 and reference) [19]. From a technological point of view, such behaviour could induce a detrimental effect in the mechanical stability of the anode side due to electrode bending and/or interfacial stress under reducing conditions. Similar effects are very well known in other common SOFCs materials, such as alkaline-earth doped lanthanum chromite or rare-earth doped ceria [30,31], and therefore mitigation strategies should be design to solve them.
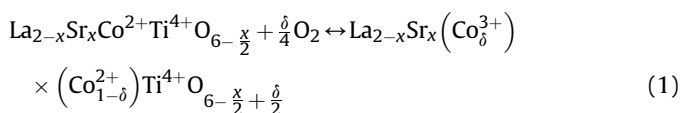
For low levels of oxygen release, i.e. for $0 \le x \le 0.20$, oxygen seems to be preferentially removed from O(3) positions which correspond to those located in the La/Sr layers (Table S4 and Fig. 1a) whereas O(1) and O(2) positions (those in the Co and Ti layers) remain fully occupied. Interestingly, for oxides with $x > 0.2$ which lose more oxygen upon reduction, oxygen is removed from the 3d-metal planes, O(2) positions (Table S4 and Fig. 1b), instead from the A-cation layers. This ensures a sufficient high coordination environment for A-cations compatible with B-cations in square-pyramids.

Finally, the octahedra tilting angles increase upon reduction (Tables S3 and S4) due to the larger size of Co^{2+} in comparison to Co^{3+} which results in a worse matching of the A–O and B–O distances evidenced by a lower tolerance factor in the reduced materials (less than unity in all cases).

3.2. Electrical properties

The dependence of the total conductivity (σ_{total}) of La$_{2-x}$SrxCoTiO$_6$ compounds on the oxygen partial pressure (pO_2) at 1173 K is displayed in Fig. 8 (data in the pO_2 range $\sim 10^{-13}$ to $\sim 10^{-4}$ atm are not shown as it is not possible to obtain reliable pO_2 values in this range due to saturation effects of YSZ sensor) [32]. All samples but the non-doped one, La$_2$CoTiO$_6$, exhibit very similar behaviour in the whole studied pO_2-range.

At reducing conditions, (flowing 5%H$_2$:Ar at 1173 K), oxygen vacancies are created due to almost full reduction of Co^{3+} to Co^{2+} (see Table S2). As oxygen partial pressure increases reoxidation of Co^{2+} takes place accordingly to the reaction given in Equation (1):

$$La_{2-x}Sr_xCo^{2+}Ti^{4+}O_{6-\frac{x}{2}} + \frac{\delta}{4}O_2 \leftrightarrow La_{2-x}Sr_x\left(Co_\delta^{3+}\right)$$
$$\times \left(Co_{1-\delta}^{2+}\right)Ti^{4+}O_{6-\frac{x}{2}+\frac{\delta}{2}} \tag{1}$$

Conductivity increases as pO_2 increases following a linear power law with slope $\sim \frac{1}{4}$ as oxidation progresses, within $\sim 10^{-22}$ to $\sim 10^{-12}$ atm range. This is indicative of p-type conduction as the main transport mechanism, Co^{3+}, being considered a hole defect-like [Co$_{Co}^\bullet$] or alternatively as due to the formation of holes in the conduction band. This process can be expressed according to the equilibrium given in Equation (2):

$$V_O^{\bullet\bullet} + 1/2O_2 \leftrightarrow O_O^x + 2h^\bullet \tag{2}$$

where $V_O^{\bullet\bullet}$ denotes oxygen vacancies present under reducing conditions and $h^\bullet$ denotes holes in the conduction band originated by the oxidation process. The equilibrium constant is given by Equation (3):

$$K_O = \frac{[O_O^x][h^\bullet]^2}{[V_O^{\bullet\bullet}]pO_2^{1/2}} \tag{3}$$
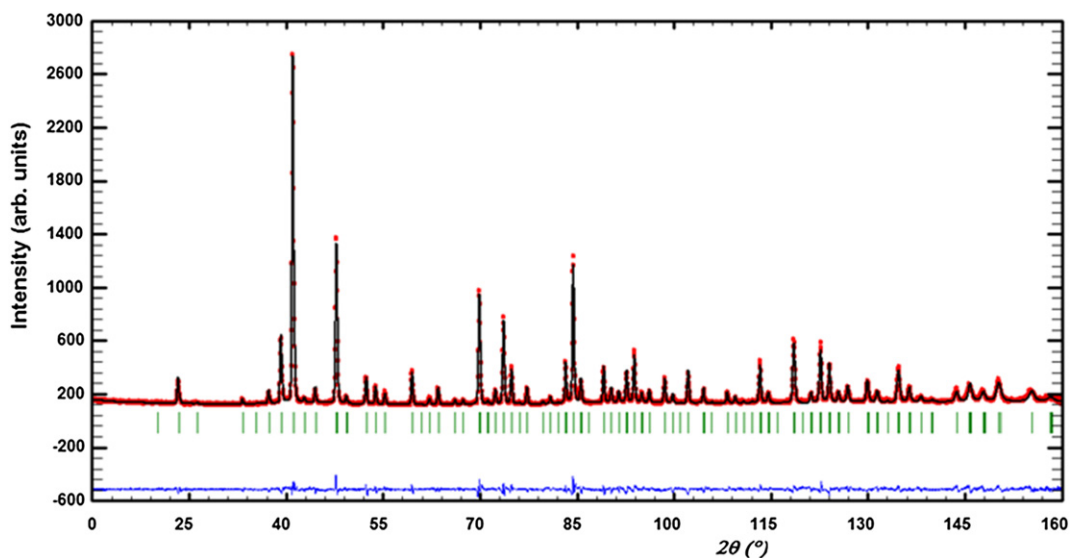

Fig. 7. Experimental (red circles) and calculated (black continuous line) NPD patterns (and their difference, blue line at the bottom) for reduced La$_{1.70}$Sr$_{0.30}$CoTiO$_{6-\delta}$ assuming S.G. Pnma. The green vertical bars indicate the positions of the Bragg peaks of this phase. (For interpretation of the references to colour in this figure legend, the reader is referred to the web version of this article.)
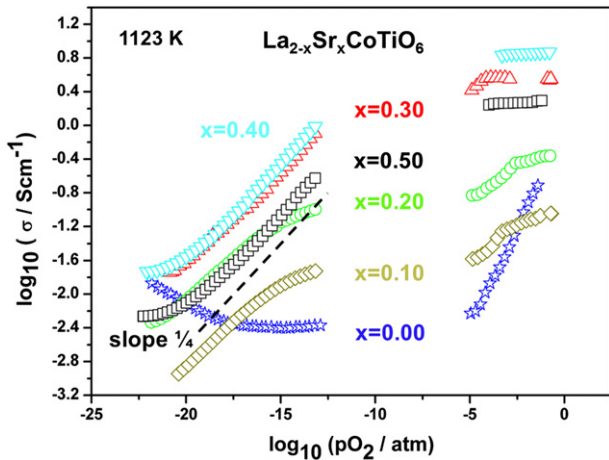
Fig. 8. Total conductivity of $La_{2-x}Sr_xCoTiO_6$ ($x = 0$, 0.10, 0.20, 0.30, 0.40 and 0.50) at 1123 K as a function of the oxygen partial pressure, pO_2.

where $[O_O^x]$ can be considered as a constant and $[h^\bullet] = \delta$, then:

$$\delta = (K_O'[V_O^{\bullet\bullet}])^{1/2} pO_2^{1/4} \tag{4}$$

On the other hand $[V_O^{\bullet\bullet}] = x/2 - \delta/2$ can be considered also constant at low pO_2, in as much as $x/2 >> \delta/2$. And therefore, the conductivity can be expressed by Equation (5):

$$\sigma_{elec} \propto \delta = (K_O'')^{1/2} pO_2^{1/4} \tag{5}$$

In which the concentration of charge carriers, $[h^\bullet]$, has been identified as that of Co^{3+} which is being created upon oxidation with a limit corresponding to the degree of aliovalent substitution La^{3+}/Sr^{2+}.

At high pO_2, the quantity of holes reaches a maximum as the oxygen substructure is completed. This situation corresponds to the compounds prepared under air that are more precisely described by the formula for $La_{2-x}Sr_x(Co^{3+})_x(Co^{2+})_{1-x}TiO_6$. Therefore as saturation is reached, a pO_2-independent regime for conductivity is anticipated. Experimental evidence of this behaviour is clearly seen in the high-pO_2 region shown in Fig. 8. Remarkably, the Sr-substituted materials exhibit a quite high and stable non-pO_2 dependent conductivity under mild reducing conditions.

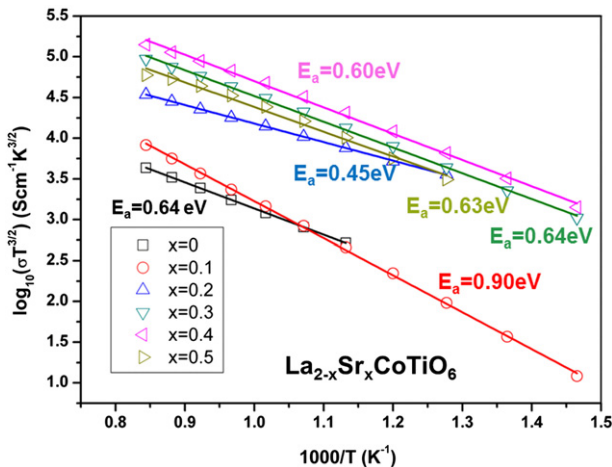**Fig. 9.** Non-adiabatic small-polarons hopping fits to the total conductivity for $La_{2-x}Sr_xCoTiO_6$ ($x = 0$, 0.10, 0.20, 0.30, 0.40 and 0.50).

Regarding the variation of conductivity as a function of x in the $La_{2-x}Sr_xCoTiO_6$ series, according to this model of p-type conduction, at a given pO_2 the conductivity should increase as the concentration of charge carriers, i.e. holes, increases. Since substitution of La^{3+} by Sr^{2+} implies an increase of the hole concentration under oxidizing conditions, an enhancement of conductivity with x is expected, the highest value in the herein presented series being expected for the $La_{1.50}Sr_{0.50}CoTiO_6$ oxide. This trend is actually observed in Fig. 8 (more clearly in Fig. 9 which depicts the total conductivity Arrhenius plot in air, see below). However, this sample with $x = 0.50$ exhibits an unexpectedly low conductivity. In this context significant changes in the conduction properties of perovskites as consequence of a local charge order that induces the localization of the charge carries (holes) or widening of the band-gap have been reported [33,34]. SAED and HREM showed that the $La_{1.50}Sr_{0.50}CoTiO_6$ compound presents a very complex microstructure, including short-range ordering phenomena (Figs. 4–6), not observed for other members of the series. As a consequence the electrical conductivity of the $x = 0.50$ member is slightly lower from what it is expected on the basis of the general trend observed along the $La_{2-x}Sr_xCoTiO_6$ series.

On the other hand, the non-doped material, La_2CoTiO_6, presents some important differences in its conductivity as a function of pO_2 (Fig. 8). In the low pO_2 region (from 10^{-22} to 10^{-17} atm), the conductivity decreases as pO_2 increases denoting an n-type electronic conduction. Associated to this conduction mechanism should be the reduction of any redox-active ion; in this case the most plausible process seems to be reduction of Ti^{4+} to Ti^{3+} [35]. Thus, the equilibrium expressed by Equation (6) holds:

$$O_O^x \leftrightarrow 1/2O_2 + V_O^{\bullet\bullet} + 2e' \tag{6}$$

from which the conductivity can be obtained as:

$$\sigma_{elec} \propto [e'] = K_e^{1/2}[V_O^{\bullet\bullet}]^{-1/2} pO_2^{-1/4} \tag{7}$$

According to Fig. 8, a $(pO_2)^{(-1/4)}$ power-law dependence of conductivity is observed. The experimental finding only agrees with Equation (7) if $[V_O^{\bullet\bullet}]$ is constant. This requires that a relatively high number of vacancies are present when compared to those created according to Equation (6). The most plausible explanation for this is to assume some A-site off-stoichiometry, quite common in perovskites [25] which accounts for the electrical properties of similar materials such as Sr_2EuNbO_6 [36]. Even more, this assumption is really needed to interpret the complete conductivity behaviour in the full pO_2 region.

In the intermediate pO_2-range (from 10^{-20} to 10^{-9} atm) conductivity remains almost constant. This is commonly associated to an ionic conduction mechanism due to mobile oxygen-vacancies, again A-site off-stoichiometry seem to be responsible for the existence of such anion vacancies. The degree of A-site non-stoichiometry as well as the amount of oxygen vacancies originated upon reduction seems to be very low since they are not detected by NPD (Tables S1 and S2).

Finally, in the high-pO_2 region (from 10^{-3} atm to ambient atmosphere), the conductivity increases with the oxygen partial pressure in a similar manner than previously observed for the Sr-substituted compounds; this behaviour suggests a p-type conductivity. This is associated to the presence of Co^{3+} in this non-substituted material pointing again to the existence of some A-site off-stoichiometry. Interestingly, in a previous paper we determined by chemical titration the presence of some amount of trivalent cobalt in the starting material [19]. On the other hand, conductivity

follows a $(pO_2)^n$ power-law dependence with $n \sim 0.4$, indicative of an out-of-equilibrium situation, probably associated to oxygen diffusion.

Fig. 9 shows the temperature dependence of σ_{total} for the La$_{2-x}$Sr$_x$CoTiO$_6$ ($0 \leq x \leq 0.50$) series under air (oxidizing conditions) as obtained by IS using the interception of the inductive response with the real Z′ axis of the Nyquist plots. No electrode response (at low frequency) indicative of diffusion or charge transfer phenomena has been found. Thus, conduction in these materials is dominated by the electronic contribution. A noticeable enhancement of conductivity with the substitution level is observed, except for La$_{1.50}$Sr$_{0.50}$CoTiO$_6$ which displays an unexpected low conductivity. This has been discussed above as due to microstructural and short-range order, as determined by SAED and HREM. As shown in Fig. 9 the electrical conductivity increases with temperature, as expected for a semiconducting-like behaviour. However, the Arrhenius plot $\log(\sigma)$ vs. T^{-1} gives a quite poor fit of the experimental data (Figure S3). This, together with the conductivity increase under oxidizing conditions shown in Fig. 8, suggests that these materials should exhibit a temperature activated small-polarons-hopping transport mechanism due to diffusion of p-type carriers (holes) [37,38] associated to the existence of Co^{2+} and Co^{+3} ions in the structure.

The mobility of small-polarons can be explained using two approaches: adiabatic or non-adiabatic conditions. In the first case, the carrier jumps to an adjacent unoccupied site whenever an atomic displacement assists this jump; in the non-adiabatic mechanism the polaron jumps only occasionally due a favourable atomic configuration [39,40]. In principle, it is possible to differentiate between these two mechanisms, adiabatic or non-adiabatic, analysing the temperature dependence of σ_{total} [38]. The plot of $\log(\sigma T)$, for the adiabatic mechanism, or $\log(\sigma T^{3/2})$, for the non-adiabatic one, versus T^{-1} must show a straight line with the slope related to the activation energy (E_a) of the small-polarons hopping process. Although it is difficult to distinguish between the two regimes from this simple graphical analysis, slightly better fits are obtaining using the non-adiabatic model in all cases. Therefore, the electrical conduction of these materials seems to occur via the non-adiabatic small-polaron mechanism. The E_a along the whole series is low and similar indicating that the same conduction mechanism operates and that the local environments of polarons are similar in all samples.

Since the material with $x = 0.40$, La$_{1.60}$Sr$_{0.40}$CoTiO$_6$, displays the highest electrical conductivity of the series, it was selected as an example to assess the electrochemical performance of the family. NPD revealed that La$_{2-x}$Sr$_x$CoTiO$_6$ materials are stable under oxidizing and reducing conditions at high temperatures. Besides, chemical compatibility tests revealed that they do not react or decompose when heated with YSZ (used as component of the electrodes of SOFCs) at temperatures as high as 1373 K either in oxidizing (air) or reducing (5%H$_2$:Ar) conditions. Figures S4a and S4b show the XRD patterns corresponding to a 1:1 w:w mixture of La$_{1.60}$Sr$_{0.40}$CoTiO$_6$ and YSZ treated under oxidizing and reducing and atmospheres at 1373 K for 15 h, respectively. No decomposition or reaction occurs, suggesting that these materials could be used in SOFC either in the cathode or in the anode side.

Preliminary electrochemical tests performed on symmetrical cells revealed that La$_{1.60}$Sr$_{0.40}$CoTiO$_6$-based electrodes exhibit polarization resistances of typically 0.8 Ω cm^2 at 1073 K in oxygen, which is fairly similar to the values obtained for LSM-based cathodes, e.g. 0.5 Ω cm^2 [41]. It should be noted that the polarization resistance exhibits an Arrhenius-like dependence (Fig. 10), i.e. the electrochemical response is thermally activated and shows E_a values of 1.83 eV. These results are particularly
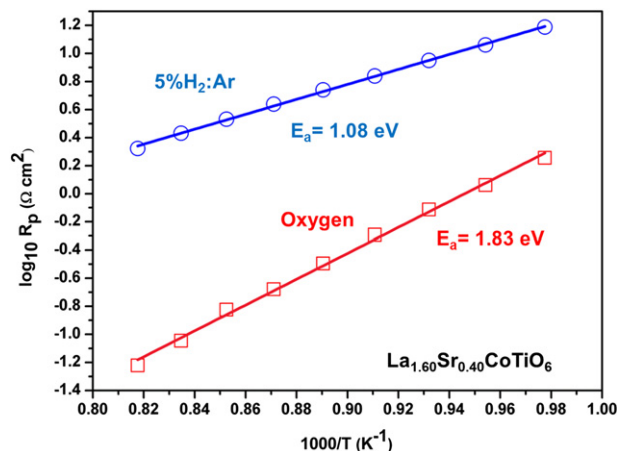
Fig. 10. Temperature dependence of the polarization resistance of La$_{1.60}$Sr$_{0.40}$CoTiO$_6$ symmetric cells under reducing (anode) and oxidizing (cathode) conditions.

encouraging after evaluating the electrode microstructure by SEM (Fig. 11).

The cross section views of the cells evaluated reveal a good adherence between the electrolyte and the electrodes. However, the degree of porosity may not be adequate to facilitate the gas transient towards the active sites and also it should be noted that the particle size and distribution is rather heterogeneous, which may certainly have a negative impact on the electrode response. Consequently, the optimization of the electrodes microstructure may lead to polarization values in the range of the target values demanded by SOFC manufacturers, i.e. 0.1–0.15 Ω cm^2.

In the symmetrical cell measurements performed under flowing 5%H$_2$:Ar mixture the polarization was larger, e.g. 8.9 Ω cm^2 at 1073 K, the activation energy being 1.08 eV. The improvement of the electrodes microstructure, for instance via the use of ceria-based composites as reported by Marina et al. in perovskite titanates [42], could enhance their electrochemical performance.

The Co-based oxides La$_{2-x}$Sr$_x$CoTiO$_6$ show significantly improved electrochemical performances with respect to the analogous compounds La$_{2-x}$Sr$_x$NiTiO$_{6-\delta}$ previously reported [43]. Thus, La$_{2-x}$Sr$_x$CoTiO$_6$ perovskites are potentially useful materials for SOFCs components, particularly in the cathode side. The enhancement of the electrical conductivity by widening the substitution range up to $x = 1.00$ and the control and improvement of the
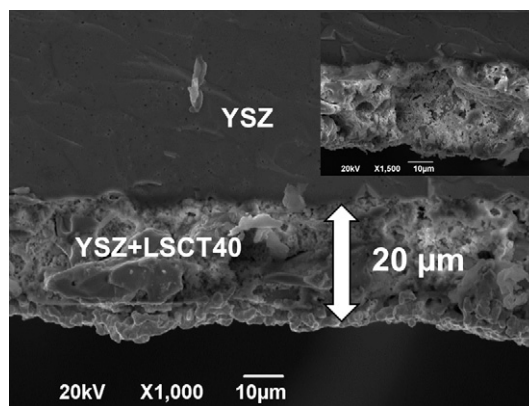
Fig. 11. SEM micrograph of the La$_{1.60}$Sr$_{0.40}$CoTiO$_6$/YSZ electrode prepared at 1373 K overnight. The inset shows a detail of the heterogeneous particle size, grain distribution and porosity.

electrode microstructure are promising approaches that we are currently exploring and results will be published soon.

4. Conclusion

The $La_{2-x}Sr_xCoTiO_6$ ($0 \leq x \leq 0.50$) series show a double perovskite structure with unit cell $\sqrt{2}a_p \times \sqrt{2}a_p \times 2a_p$. The symmetry changes from monoclinic ($P2_1/n$) for low Sr contents, $x \leq 0.20$, to orthorhombic (Pnma) for $x > 0.20$; however, the tilting system $a^-a^-c^+$ is equivalent for both symmetries. The monoclinic cell is adopted as a result of cobalt and titanium ordering on the B′ and B″ sites, whereas substitution of La^{3+} by Sr^{2+} provides the driving force for disordering cations in the B-site resulting in the orthorhombic symmetry.

The substitution of La^{3+} by lower valence Sr^{2+} is experimentally observed to be charge-compensated by the oxidation of Co^{2+} to Co^{3+} the oxygen substructure being complete as revealed by high resolution neutron diffraction.

The electrical behaviour of the $La_{2-x}Sr_xCoTiO_6$ ($0 < x \leq 0.50$) system is dominated by p-type electronic conduction in the whole pO_2 range measured, as indicated by a $+1/4$ power-law dependence of the conductivity on pO_2. The analysis of the thermal evolution of total conductivity allows proposing that electrical conduction in these materials occurs via the non-adiabatic-hopping of small-polarons mechanism.

The p-type charge-carrier concentration increases with increasing acceptor-dopant content and consequently the electrical conductivity displays the same trend, except for the $x = 0.50$ material which shows an unexpectedly low conductivity due to microstructural and short-range ordering effects evidenced by SAED and high resolution electron microscopy. Thus, the maximum conductivity is reached for the $La_{1.60}Sr_{0.40}CoTiO_6$ oxide. For this reason this compound was selected as example to study the electrochemical performance of the whole family. Prior to these studies, the analysis of mixtures with YSZ at different temperatures showed that it is chemically compatible with YSZ, the most used electrolyte for SOFC at temperatures as high as 1373 K, in both oxidizing and reducing atmospheres.

The preliminary evaluation of the electrode performance reveals that $La_{1.60}Sr_{0.40}CoTiO_6$-based electrodes exhibit polarization resistances quite similar to the values obtained for LSM-based cathodes; on the contrary the performance in reducing conditions is noticeably worse. The electrochemical behaviour of this oxide as cathode is particularly encouraging since the electrode microstructure has not been optimized; it is expected that $La_{1.60}Sr_{0.40}CoTiO_6$-based cathodes with improved microstructure may perform at least similarly to state-of-the-art materials in real SOFCs.

References

[1] R.M. Ormerod, Chemical Society Reviews 32 (2003) 17.
[2] Z. Liu, M.-F. Han, W.-T. Miao, Journal of Power Sources 173 (2007) 837–841.
[3] R. Robert, L. Bocher, M. Trottmann, A. Reller, A. Weidenkaff, Journal of Solid State Chemistry 179 (2006) 3893–3899.
[4] M.A. Peña, J.L.G. Fierro, Chemical Reviews 101 (2001) 1981–2018.
[5] S. Jiang, Journal of Materials Science 43 (2008) 6799–6833.
[6] S.B. Adler, Solid State Ionics 135 (2000) 603.
[7] E. Iguchi, K. Ueda, H. Nakatsugawa, Journal of Physics: Condensed Matter 10 (1998) 8999.
[8] P.M. Raccah, J.B. Goodenough, Journal of Applied Physics 39 (1968) 1209.
[9] A. Petric, P. Huang, F. Tietz, Solid State Ionics 135 (2000) 719–725.
[10] H. Nakatsugawa, E. Iguchi, Journal of Physics: Condensed Matter 11 (1999) 1711.
[11] A.N. Petrov, O.F. Kononchuk, A.V. Andreev, V.A. Cherepanov, P. Kofstad, Solid State Ionics 80 (1995) 189.
[12] A. Mineshige, M. Kobune, S. Fujii, Z. Ogumi, M. Inaba, T. Yao, K. Kikuchi, Journal of Solid State Chemistry 142 (1999) 374–381.
[13] C. Wagner. Part 1, Progress in Solid State Chemistry 10 (1975) 3–16.
[14] W. Preis, E. Bucher, W. Sitte, Journal of Power Sources 106 (2002) 116–121.
[15] C.H. Chen, H.J.M. Bouwmeester, R.H.E. van Doorn, H. Kruidhof, A.J. Burggraaf, Solid State Ionics 98 (1997) 7–13.
[16] T. Wei, Q. Zhang, Y.-H. Huang, J.B. Goodenough, Journal of Materials Chemistry 22 (2012) 225–231.
[17] L. Ortega-San Martin, J.P. Chapman, L. Lezama, J. Sanchez-Marcos, J. Rodriguez-Fernandez, M.I. Arriortua, T. Rojo, Journal of Materials Chemistry 15 (2005) 183–193.
[18] T. Sugahara, M. Ohtaki, Applied Physics Letters 99 (2011) 062107.
[19] M. Yuste, J.C. Perez-Flores, J.R. de Paz, M.T. Azcondo, F. Garcia-Alvarado, U. Amador, Dalton Transactions 40 (2011) 7908–7915.
[20] J. Rodríguez-Carvajal, Physica B: Condensed Matter 192 (1993) 55–69. The program and manual can be found at, http://www.ill.eu/sites/fullprof/.
[21] J.C. Perez Flores, C. Ritter, D. Perez-Coll, G.C. Mather, F. Garcia-Alvarado, U. Amador, Journal of Materials Chemistry 21 (2011) 13195–13204.
[22] J.C. Ruiz-Morales, J. Canales-Vázquez, J. Peña-Martínez, D.M. López, P. Núñez, Electrochimica Acta 52 (2006) 278–284.
[23] A. Glazer, Acta Crystallographica Section B 28 (1972) 3384–3392.
[24] G. King, P.M. Woodward, Journal of Materials Chemistry 20 (2010) 5785–5796.
[25] R.H. Mitchell, Perovskite: Modern and Ancient, Almay Press Inc., Ontario (Canada), 2002.
[26] C. Meneghini, S. Ray, F. Liscio, F. Bardelli, S. Mobilio, D.D. Sarma, Physical Review Letters 103 (2009) 046403.
[27] R.D. Shannon, Acta Crystallographica Section A 32 (1976) 751–767.
[28] T. Shimada, J. Nakamura, T. Motohashi, H. Yamauchi, M. Karppinen, Chemistry of Materials 15 (2003) 4494–4497.
[29] Á. Vegas, M. Mattesini, Acta Crystallographica Section B 66 (2010) 338–344.
[30] C.P. Khattak, D.E. Cox, Materials Research Bulletin 12 (1977) 463–471.
[31] M. Mogensen, N.M. Sammes, G.A. Tompsett, Solid State Ionics 129 (2000) 63–94.
[32] M.J. Rampling, G.C. Mather, F.M.B. Marques, D.C. Sinclair, Journal of the European Ceramic Society 23 (2003) 1911–1917.
[33] J.M.D. Coey, M. Viret, S. von Molnár, Advances in Physics 48 (1999) 167–293.
[34] H.W. Eng, P.W. Barnes, B.M. Auer, P.M. Woodward, Journal of Solid State Chemistry 175 (2003) 94–109.
[35] Y. Yamada, O. Hino, S. Nohdo, R. Kanao, T. Inami, S. Katano, Physical Review Letters 77 (1996) 904–907.
[36] Z. Maupoey, M.T. Azcondo, U. Amador, A. Khun, J.C. Perez Flores, J. Romero de Paz, N. Bonanos, F. García-Alvarado, Journal of Materials Chemistry (2012).
[37] D. Emin, T. Holstein, Annals of Physics 53 (1969) 439–520.
[38] R. Koc, H.U. Anderson, Journal of the European Ceramic Society 15 (1995) 867–874.
[39] M. Viret, L. Ranno, J.M.D. Coey, Physical Review B 55 (1997) 8067–8070.
[40] S. Chatterjee, P.H. Chou, C.F. Chang, I.P. Hong, H.D. Yang, Physical Review B 61 (2000) 6106–6113.
[41] J.D. Kim, G.D. Kim, J.W. Moon, Y.I. Park, W.H. Lee, K. Kobayashi, M. Nagai, C.E. Kim, Solid State Ionics 143 (2001) 379.
[42] O.A. Marina, L.R. Pederson, in: J. Huijsmans (Ed.), Proc. 5th European Solid Oxide Fuel Cell Forum, Switzerland, 2002, pp. 481–489.
[43] J.C. Pérez-Flores, C. Ritter, D. Pérez-Coll, G.C. Mather, J. Canales-Vázquez, M. Gálvez-Sánchez, F. García-Alvarado, U. Amador, International Journal of Hydrogen Energy 37 (2012) 7242–7251.